



Densification, mechanical behaviors, and machining characteristics of 316L stainless steel in hybrid additive/subtractive manufacturing

Yuying Yang¹ · Yadong Gong¹ · Shuoshuo Qu¹ · Hualong Xie¹ · Ming Cai¹ · Yunchao Xu¹

Received: 11 August 2019 / Accepted: 28 January 2020 / Published online: 14 February 2020
© Springer-Verlag London Ltd., part of Springer Nature 2020

Abstract

Directed energy deposition (DED) is capable of manufacturing high-density and complex metal components, whereas traditional machining methods are limited in these regards. Nevertheless, the fabrication of parts with DED that have accurate dimensions and geometries as well as acceptable surface states is a concern, as these factors are inferior to those of traditionally machined components. Therefore, the application of parts fabricated with DED is restricted. Thus, the hybrid additive/subtractive manufacturing (HASM) method has been exploited to comprehensively utilize the advantages of both. In this paper, the HASM method was used to fabricate bulk parts with four different scanning strategies (alternating the orientation of subsequent layers by 0°, 45°, and 90° and island scanning are referred to as an X-scan, a Rot-scan, an XY-scan, and an Island-scan, respectively) followed by subtractive milling to gain a smooth surface with a determined thickness for the next scanning and deposition period until the parts were completely finished. The influence of the scanning strategy on the densification level and mechanical behavior of the specimens fabricated with HASM was studied. The results show that the specimens fabricated with the $7 \times 7 \text{ mm}^2$ island scan with short scan vector lengths showed a higher densification than the specimens fabricated using long scan vector lengths (the three methods mentioned above). Finally, to obtain a fine surface finish, the influence of the feed per tooth (f_z) on the surface quality of a 316L stainless steel during the milling process that occurs during the HASM process was also investigated. The result shows a f_z of 0.25 mm yielding the minimum surface roughness value among the samples observed herein, which implies that the surface quality was better than that of the other studied conditions.

Keywords Hybrid additive/subtractive manufacturing · Densification level · Mechanical behaviors · Feed per tooth · Machined surface roughness

1 Introduction

During the additive manufacturing (AM) fabrication of metallic alloys, three-dimensional parts are fabricated in a layer-by-layer pattern through local delivery of metal powder or wire feedstock, melting of the feedstock by means of a laser or electron beam heat source, and quick solidification of the molten material [1–4]. AM combines computer graphics, digital information and engineering, laser technology and material processing, as well as forming technology to fabricate the part. Directed energy deposition (DED) belongs to a class of high-tech AM

technologies that operate based on rapid prototyping combined with coaxial powder feeding laser cladding technology [5–7]. It provides a new method for manufacturing complex structural parts, thus making it a hot research topic and concern in related fields due to its advantages of a short cycle, decreased fabricating costs, no need for dies, and high compactness. However, as a relatively new and continuous improvement technology, not all the disadvantages have been solved. First, residual stress and deformation are introduced into the parts due to a large temperature gradient during the AM process, and second, the surface quality and accuracy of the components do not meet requirements due to a stair-step effect [8, 9]. Traditional subtractive manufacturing (SM) processes, such as milling and grinding, can improve the surface quality of parts, which is a relatively complete solution and currently plays an important role in the metal manufacturing industry [10, 11]. Hopefully, near-net-shaped metallic components can achieve relatively good surface quality through subsequent milling technology.

✉ Yadong Gong
gongyd@mail.neu.edu.cn

¹ School of Mechanical Engineering and Automation, Northeastern University, Shenyang 110819, China

Austenitic stainless steels, such as 316L stainless steel (316L SS), are well known for their weldability, excellent corrosion resistance (especially pitting resistance), temperature resistance, and creep resistance [12, 13]. Owing to these characteristics, they have been extensively used in aerospace, machinery, and biomedical engineering applications. For example, 316L SS parts with complex structures, such as aviation engine blades, can be repaired and remanufactured by hybrid additive and subtractive manufacturing (HASM), which consists of additive manufacturing DED followed by a subtractive manufacturing (SM) milling process to improve the surface state. Research on HASM is attracting increasing attention. These previous fundamental studies provide a firm foundation for further study, and additional HASM processes have been explored [14–17]. In this context, HASM, which combines DED with coaxial powder feeding and conventional five-axis CNC milling, can be used in exploratory studies to finish real functional metallic components instead of the single additive manufacturing technology of DED or selective laser melting or sintering (SLM or SLS) to directly fabricate near-net shaped metal components. In other words, this technology can resolve the aforementioned low surface quality of components fabricated with DED only. To obtain improved parts fabricated with HASM, the additive DED process still needs to be controlled. Due to the complex melting-solidification process that occurs because of interactions with a laser beam, substrate, and powder stream in the DED process, several factors, such as the laser powder, scanning speed, feeding rate, and scanning strategy, influence the microstructure and mechanical properties, such as the tensile behavior and Vickers hardness of the final parts. Wei et al. [18] demonstrated that the porosity, microstructure, and attendant mechanical properties of an AlSi10Mg alloy can be adjusted by the processing parameters during the selective laser melting (SLM) process. The results show that the densification behavior is related to the energy density of the laser beam and the mechanical behavior can be improved by increasing the level of densification. Qiu et al. [19] investigated the effect of the laser power, scanning speed, and post-SLM heat treatment on the porosity and microstructural development. The post-SLM heat treatment slightly impacted the tensile properties; moreover, the tensile behavior and plasticity can be achieved by adjusting the hot isostatic pressing process. AlMangour et al. [20] found that using four different scanning strategies strongly affected the porosity, microstructure, texture, and anisotropy of the components fabricated by SLM. The choices of major parameters have a fundamental effect on the final quality of parts. The improper selection of process parameters results in an uneven surface of the cladding layer; furthermore, the geometric shape of the formed parts may deviate, and unexpected defects, such as pores or cracks, may even occur. Therefore, reasonable process parameters and scanning strategies are essential to ensure the fabrication of high-precision

and high-performance parts. Moreover, to obtain a fine surface finish, reasonable milling processing parameters should also be considered. Xiong et al. [21] used optimized process parameters to fabricate a group of metal components by a hybrid plasma deposition and milling process. Moreover, the study also indicated that the feed per tooth played a vital role in the surface roughness among all the process parameters.

There have been a large number of studies about the factors for AM or SM techniques to produce certain properties and microstructures, but systematic studies of components fabricated with HASM as a function of the technical parameters to meet industrial requirements are seldom reported. In this study, during the HASM process, once a deposition cycle period (each deposition cycle period produces four layers) finished, the deposited top surface was processed to the desired thickness for further deposition by a subsequent milling process until the prescribed deposition operation was completed. Therefore, to improve the surface quality of 316L SS samples fabricated with HASM, reasonable machining parameters should be considered that use a subtractive computer numerical control (CNC) milling process during HASM. Moreover, the process conversion between DED and CNC milling can be achieved by CNC.

The aim of this paper is to enable the use of 316L SS fabricated with HASM. Appropriate process parameters, such as the scanning strategy during the DED process and feed per tooth (f_z) during SM milling that happened in the HASM process, were determined by experimental methods. First, we investigated the influence of the building scanning strategy on the mechanical properties of the 316L SS parts fabricated with HASM. To this aim, we fabricated bulk specimens with four different scanning strategies (alternating the orientation of subsequent layers by 0° , 45° , and 90° and island scanning are referred to as an X-scan, a Rot-scan, an XY-scan, and an Island-scan, respectively). Next, we evaluated the stress-strain response and fracture surface analysis and densification level. Finally, achieving the final shape with DED process methods is often difficult without post-fabrication processing, such as machining. Reasonable machining parameters, such as the f_z , should be chosen to obtain a good surface quality.

2 Experimental methods

2.1 Material and process parameters

Gas-atomized 316L stainless steel (316L SS) powder with an approximate spherical shape and the particle diameter of 10–130 μm is chosen as the deposition material. The scanning electron microscopy (SEM) picture of 316L SS powder and the chemical compositions of 316L SS powder were shown in Fig. 1 and Table 1, respectively. As can be seen from Fig. 1, a large number of small particles exist in the powder, which may

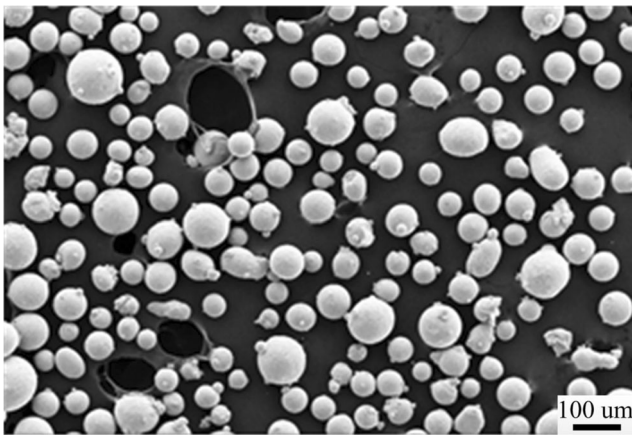


Fig. 1 SEM image of microscopy of 316L SS powders

have a negative impact on their fluidity owing to agglomeration of small particles; nevertheless, they can dramatically increase the specific surface area of the material, resulting in a high-energy absorption rate of the laser beam [22, 23]. In addition, the 40[#] steel plate with the dimension of $160 \times 160 \times 20 \text{ mm}^3$ was used as the substrate material. The chemical composition of 40[#] steel is shown in Table 2. Before the HASM experiment, the milling process and chemical cleaning are applied to clean the surface of the 40[#] steel substrate.

This work was executed on the experimental equipment of the HASM machine (SVW80C-3D) (see Fig. 2a), which is composed of the additive DED (see Fig. 2b) and the subtractive milling machining (see Fig. 2c) to manufacture the end-metal part. The detail of the process parameters are listed in Table 3. The main parts of the additive DED system is composed of a fiber laser system (IPG YLS-2000) (see Fig. 2d) with a wavelength of 1070–1080 nm, powder feeding machine (see Fig. 2e), water-cooling system, and laser head. Some main parts of the experimental equipment of the HASM are shown in Fig. 2.

2.2 Scanning strategy

Understanding the influence of the scanning strategy on the densification level of components fabricated with HASM is a complicated issue owing to the various parameters related to the scanning strategy. Changing the length, direction, and sequence of scanning vectors as well as the rotation of each subsequent layer can result in a remarkable combination of scanning strategies. In this study, the influence of the scanning

strategy on the densification level and mechanical properties was determined by building several cubic bulk specimens with dimensions of $35 \times 35 \times 35 \text{ mm}^3$ for each test case. To discuss the influence of the laser scanning direction and sequence of scanning vectors as well as the rotation of each subsequent layer on the densification level and the resulting mechanical properties, a total of three scanning strategies were implemented during the DED process portion of the HASM process, as presented in Fig. 3. Bidirectional scans of 0° (X-scan), 45° (Rot-scan), and 90° (XY-scan) are alternating scanning strategies that refer to turning the orientation of each previous layer by 0° Fig. 3a, 45° Fig. 3b, and 90° Fig. 3c, respectively. To further understand the effect of the laser scanning length on the densification level and mechanical behavior of components fabricated with HASM, a chessboard scanning strategy was introduced. The chessboard scanning strategy refers to dividing the build region into several small regions. Figure 3d shows a chessboard scan with a 90° alternating scanning strategy in each individual layer and chessboard size of $7 \times 7 \text{ mm}^2$ without shifts or rotations in adjacent chessboard blocks (Island-scan). Three specimens were fabricated with each scanning strategy by the same processing parameters. Figure 3e shows the end-metal part with dimensions of $35 \times 35 \times 35 \text{ mm}^3$.

During the DED process that occurred during the HASM process, the initial direction of each of the layers is presented by blue dashed-line arrows. The island scanning strategy started with the black solid-line arrow. The first black area was scanned, and then the process to the next black area continued until it was completely done. Then, the red areas were scanned by the laser until the whole layer was completed. The same scanning sequence was repeated in all of the following deposition layers. As shown in Fig. 3, every four layers comprised a scanning period. When a scanning period was completed, the top surface was processed by CNC milling to gain a smooth surface with a determinate thickness for the next scanning period deposition. The DED and CNC milling processes were completed until the metal part was done, and the process conversion between the DED and CNC milling was achieved by the CNC method. Finally, the side surfaces were machined by CNC milling to remove the remnants of stair steps and unmelted powder particles on the surfaces and to obtain good surface quality.

2.3 Material characterization

The relative densities were measured by the Archimedes method (the relative density values were calculated by three replicates of the same sample type), and further details on the densification method can be found in refs. [11, 20, 21]. All the 316L SS specimens fabricated with HASM were processed with traditional metallographic procedures; they were

Table 1 Chemical composition (wt.%) of 316L SS powder

| Elements (wt.%) | C | Si | Mn | P/S | Cr | Ni | Mo | Other | Fe |
|-----------------|------|------|-----|------|------|------|-----|-------|------|
| Min | 0.01 | 0.4 | 0.8 | – | 16.0 | 12.0 | 2.0 | – | Bal. |
| Max | 0.03 | 0.65 | 1.4 | 0.01 | 18.0 | 14.5 | 3.2 | 0.01 | Bal. |
| Actual | 0.02 | 0.5 | 1.2 | 0.01 | 17.0 | 13.0 | 2.5 | 0.00 | Bal. |

Table 2 Chemical composition (wt.%) of the 40[#] steel

| Elements (wt.%) | C | Si | Mn | Cr | Ni | Cu | P | S | Fe |
|-----------------|------|------|------|------|------|------|------|-------|------|
| Min | 0.37 | 0.15 | 0.50 | – | – | – | – | – | Bal. |
| Max | 0.45 | 0.35 | 0.80 | 0.25 | 0.30 | 0.25 | 0.04 | 0.045 | Bal. |

sectioned, ground, and polished to obtain the densification characteristics.

The Vickers microhardness measurements were carried out on the top and side surfaces of the specimens fabricated with HASM that were polished on either the top or side surface, respectively, and the Vickers microhardness tests used an applied load of 1000 gF using a 430SVD Vickers microhardness testing machine; at least ten indentations were performed for each test case. Finally, the Vickers microhardness values were obtained from the ten measured points at the top and side surfaces of each specimen.

A series of tensile specimens were fabricated with four different scanning strategies. The tensile testing was conducted on a WDW-100E electronic universal material testing machine according to the GB/T228.1-2010 test standard. Thin-walled samples 2 mm in thickness, 16 mm in gauge length, and 30 mm in total length were prepared for tensile testing at room temperature, and three tensile samples were tested to calculate the average value under the same conditions to reduce the measurement error.

The machined surface morphology and surface roughness that formed as a result of the milling process that occurred

during the HASM process were measured with a digital microscope (VHX-1000E) and MICROMEASURE 3D surface profiler, respectively. The parameter Sa represents the surface arithmetic average error, and Sz is the maximum altitude deviation. In fact, Sa is analogous to Ra, which is a class that extends Ra. However, the difference between Sa and Ra is that the Sa data occurs in a reference plane rather than in a line. Further details relating to this testing case can be seen elsewhere [24–26]. To decrease the measurement error, at least five measurements were tested under each condition. Finally, the average of the practical measurement was considered a statistical value.

3 Results and discussion

3.1 Densification level

The density of the specimens fabricated with HASM processes that used various scanning strategies was measured by means of the Archimedes method, and the results are presented in Fig. 4a. All samples were built using various scanning

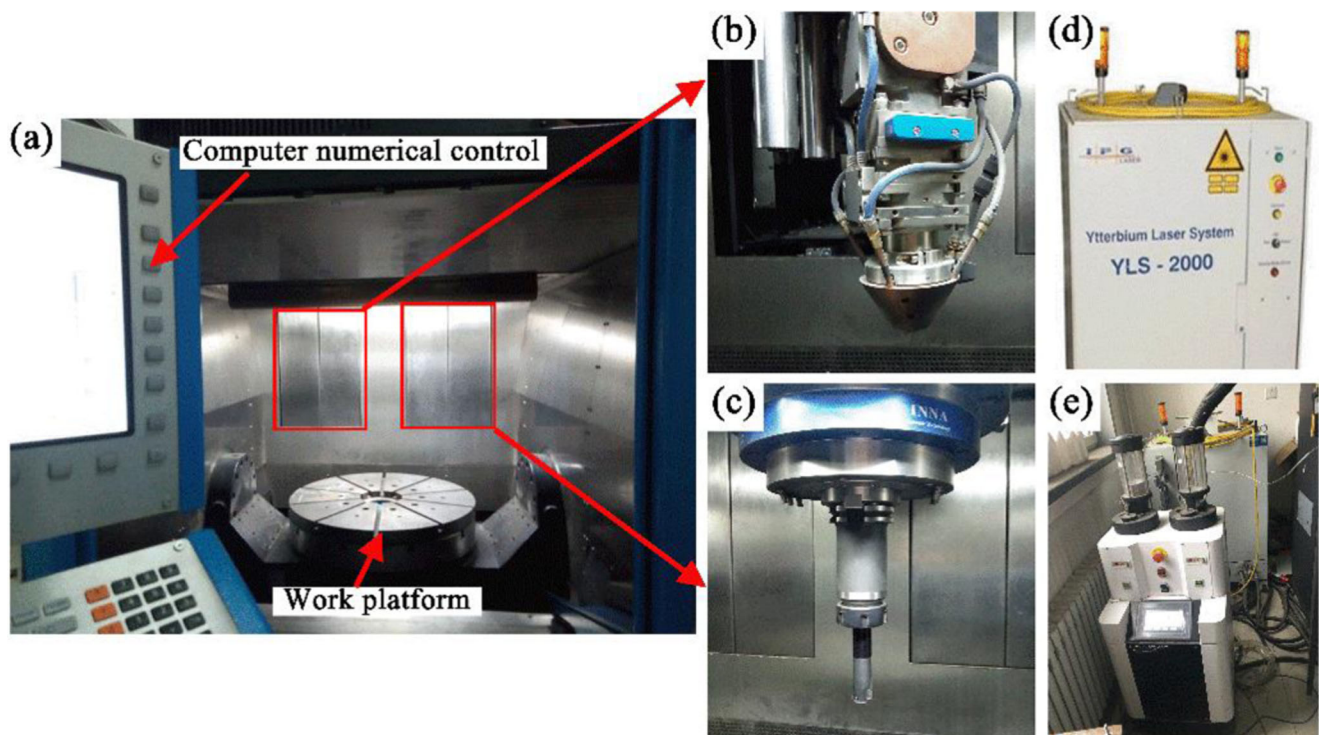


Fig. 2 Equipment of HASM experiment: **a** HASM experiment; **b** additive laser head; **c** subtractive milling head; **d** laser system; and **e** powder feeding machine

Table 3 The process parameters of HASM process

| Processing parameters | Unit | Value |
|---------------------------------|--------|----------------------|
| Laser power (P) | W | 1000 |
| Scanning speed (V) | mm/min | 440 |
| Laser beam spot size (D) | mm | 3 |
| Powder feed rate | g/min | 1 |
| Layer thickness (h) | mm | 0.5 |
| Focal length | mm | 13.5 |
| Feed per tooth (f_z) | mm | 0.2, 0.25, 0.3, 0.35 |
| Milling linear speed (V_Z) | m/min | 120 |
| Amount of axis feed (a_p) | mm | 0.5 |
| Amount of radial feed (a_e) | mm | 0.2 |

strategies with a density greater than 90%. The limited defects were composed of unmelted powder particles, pores consisting of irregular and spherical pores and thermal cracks that changed as the build direction changed during the HASM of the 316L specimens, as shown in Fig. 4b–e; the defects decreased the densification, and all specimens showed slightly different density values. To study the influence of the scan vector rotation on the density of the HASM specimens, the

orientation of the scan vectors was rotated by 0° , 45° , and 90° , and these are referred to as an X-scan, a Rot-scan, and an XY-scan, respectively. The X-scan specimen had a densification level of 96.1% (porosity of 3.9%), and a large number of pores with irregular or spherical shapes as well as hot cracks appeared in the parts fabricated with HASM; these defects mainly gave rise to discontinuous scan tracks, which then lead to interlayer pores (see Fig. 4b). The Rot-scan specimens were built with a 45° alternating scanning strategy and showed a decreasing density and had the minimum densification level herein with the highest porosity of 7.3%. A large amount of unmelted powder particles, thermal cracks, and widespread pores, including spherical pores and irregular pores, made the densification decrease to an absolute minimum of 92.7%, as shown in Fig. 4c. Such a limited densification can be attributed to poor interlayer bonding. The poor interlayer bonding was the result of the short scan vectors on the sides and the long scan vectors in the middle, thereby presenting unstable scan tracks and residual heat effects that exacerbated the formation of the pores. The XY-scan specimen had an increasing densification, resulting in a 98.2% densification compared with that from the X-scan. For the XY-scan specimens, the direction of the laser beam was perpendicular to that

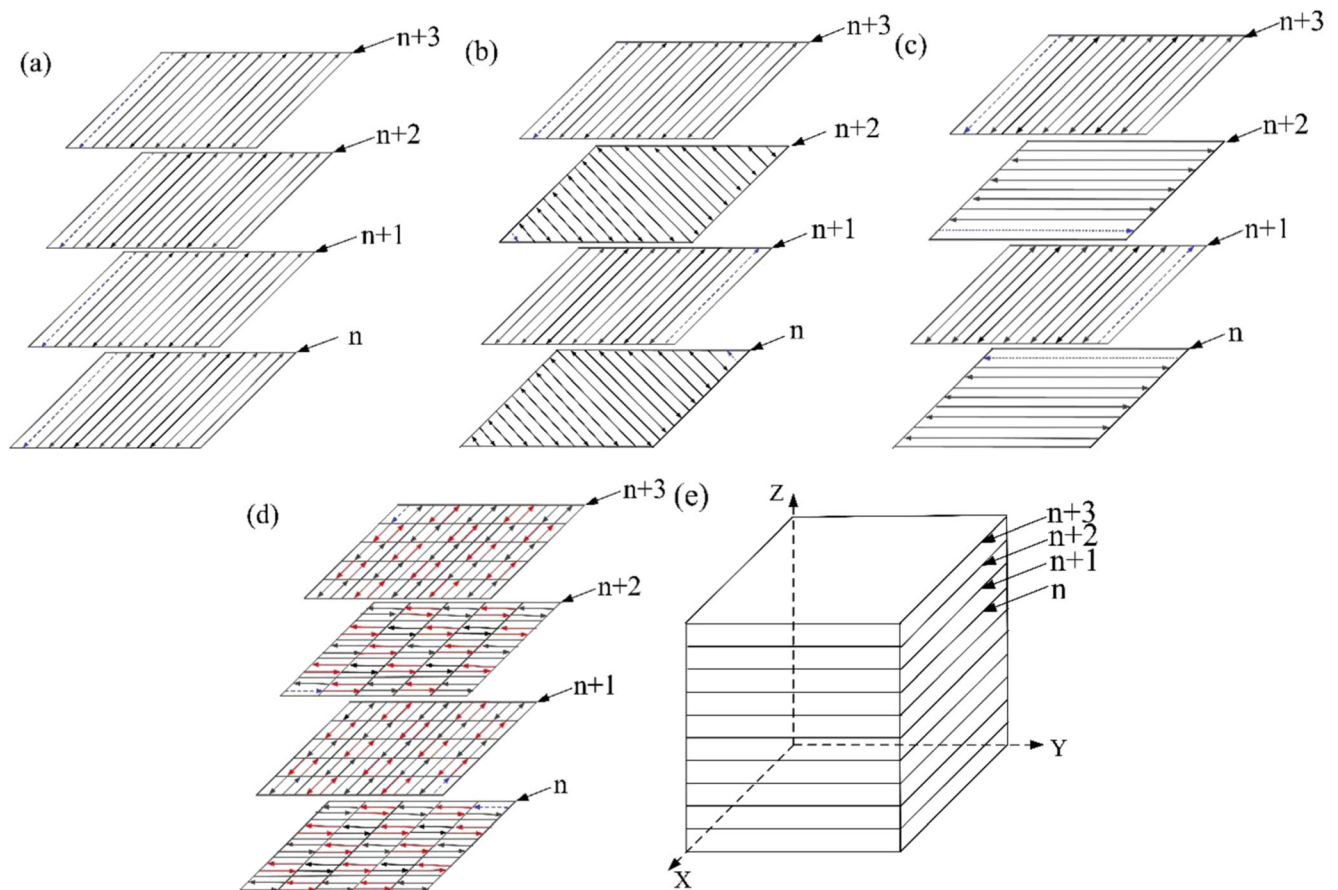


Fig. 3 Schematics of scanning strategies in HASM-fabricated 316L SS samples: **a** X-scan, **b** Rot-scan, **c** XY-scan, **d** Island-scan strategy; and **e** the end-metal part

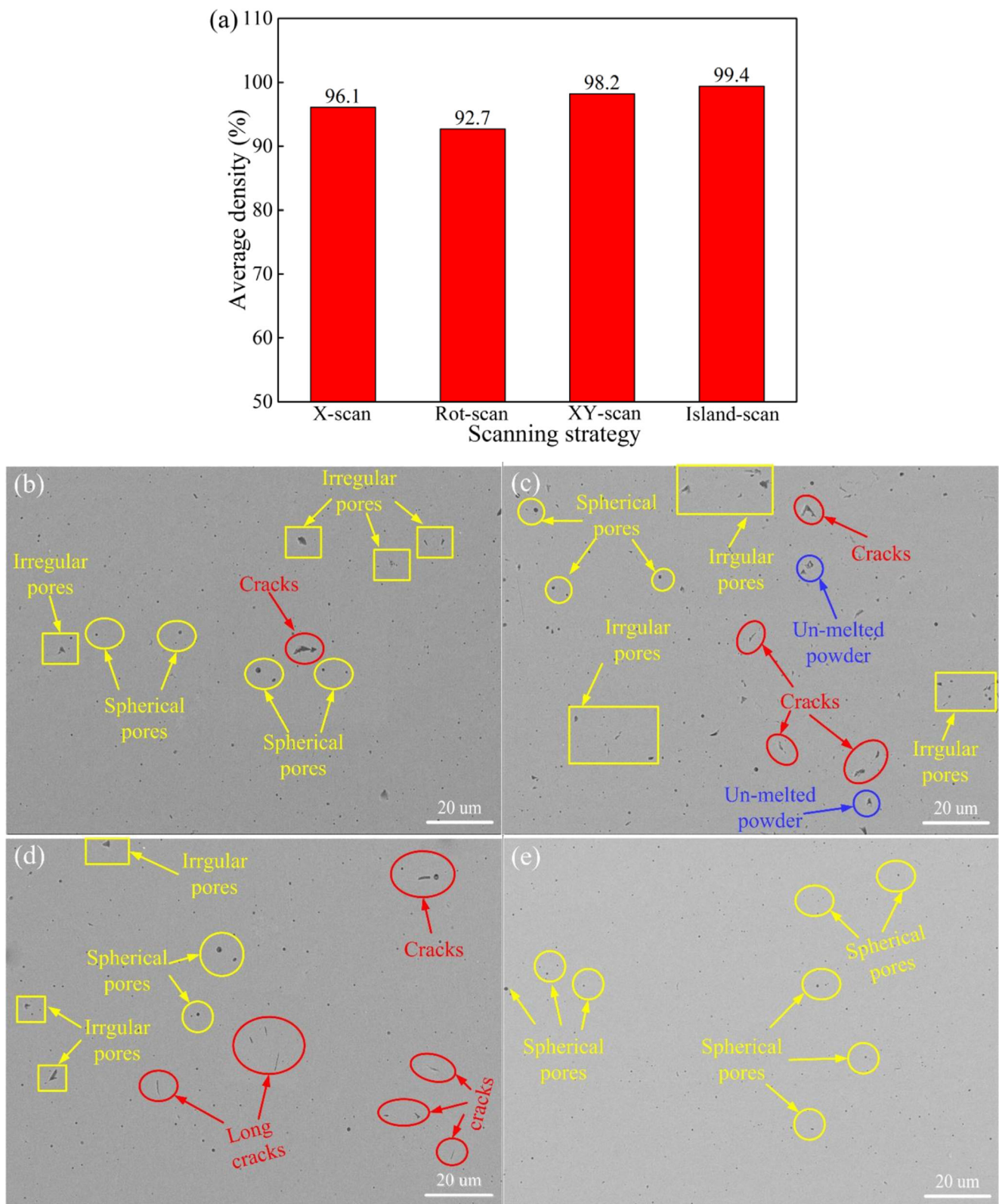


Fig. 4 a Density graphs obtained from Archimedes with variation scanning strategies consist of X-scan, Rot-scan, XY-scan, and Island-scan in HASM-fabricated 316L SS specimens; SEM images showing

the porosity in cubic specimens ($35 \times 35 \times 35 \text{ mm}^3$) manufactured at **b** X-scan, **c** Rot-scan, **d** XY-scan, and **e** Island-scan

of the previous layer, which led to a change in the heat dissipation and direction of the temperature gradient, a relatively fine microstructure with minute quantities of pores; these factors increased the densification of the fabricated samples (see Fig. 4d). These results are in good agreement with the measured results from the Archimedes method. To investigate the influence of the scan vector length on the densification, an island scanning strategy (Island-scan) was used to build the $35 \times 35 \times 35 \text{ mm}^3$ test block parts. The bulk specimen from the Island-scan separated each layer into $7 \times 7 \text{ mm}^2$ blocks, and each layer was rotated 90° with the previous layer and showed an increase in the densification. The density reached 99.4% that of all of the three alternating scanning strategies mentioned. The reason is attributed to the pores that formed during the DED process that occurred during the HASM process; the inhomogeneous temperature gradient (local heating/cooling of heat source) represents a reason for the pore formation. As a general rule, a body expands when heated and contracts when cooled. Therefore, a shorter scan vector length can reduce the porosity owing to the decreased heat input, moderate thermal gradient and effective dispersion of the heat along multiple directions rather than accumulation of the heat along the building direction [27, 28]. By and large, since the densification is considered to be related to melt flow behavior, each location in the part being fabricated suffers from a complex heat history and flow because the material first experiences rapid solidification and cooling and then remelting and cooling with each additional material layer. These complicated effects from the heating can result in heterogeneous and anisotropic densification behaviors within the parts made by HASM. However, only a few minor spherical pores were observed in the Island-scan specimen, and they were probably generated locally from the gas trapped inside the 316L SS powder, as shown in Fig. 4e. That is, the minimum hot inhomogeneity was obtained due to the reduced consolidation regions.

3.2 Mechanical properties

3.2.1 Effect of the scanning strategy on the hardness

The average Vickers hardness values obtained from the top and side surfaces of the 316L SS bulk specimens with dimensions of $35 \times 35 \times 35 \text{ mm}^3$ fabricated with HASM using different scanning strategies are presented in Fig. 5. The Rot-scan sample had the lowest hardness values herein of 206 and 225 HV on the top and side, respectively, due to the scan length on the side being short (see Fig. 3b), which resulted in an inhomogeneous residual heat transfer. The X-scan specimen had hardness values of 219 and 230 HV on the top and side, respectively. The slightly elevated values for the X-scan specimen may be a result of the increased densification level compared with that of the Rot-scan. The XY-scan specimen

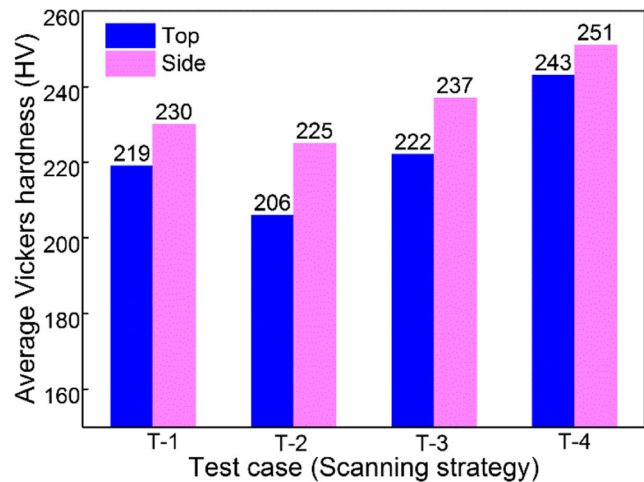


Fig. 5 Influence of scanning strategies on the Vickers hardness of the HASM-fabricated 316L SS specimens: X-scan, Rot-scan, XY-scan, and Island-scan

had an increasing hardness trend for the different scanning strategies; the specimens layers that alternated 90° with respect to the previous layer had the highest hardness values at the top and side locations with values of 222 and 237 HV, respectively; this result can be attributed to the fact that the same scan length on each layer improved the uniformity of the heat transfer. Moreover, the densification improved and the localized defects, such as pores, unmelted powders, and cracks, decreased compared with those of the X-scan or Rot-scan strategies. The hardness of the Island-scan sample increased compared with that of all three of the scanning strategies mentioned above. The Island-scan sample manufactured with the $7 \times 7 \text{ mm}^2$ island scanning strategy resulted in a hardness increase of 9.4 and 5.9% compared with that of the XY-scan specimens built with the standard 90° alternating scanning strategy, as presented in Fig. 5. Moreover, the average Vickers hardness on the top surface was lower than that on the side surfaces. Remarkable differences in the Vickers hardness values on the top and side surfaces were obtained for the specimens processed with different scanning strategies, and the results are presented in Fig. 5. The differences were due to the heterogeneous and anisotropic defects that formed because of differences in the cooling rates and inhomogeneous heat transfer among the different scanning strategies that took place during the DED portion of the HASM process. Finally, the hardness was changed by changing the scan vector direction or length because these parameters usually decide the degree of partial remelting of the previous layers. This behavior is consistent with the densification results.

3.2.2 Effect of the scanning strategy on the tensile behavior

A typical engineering stress-strain curve for the four 316L SS HASM scanning strategies consisting of three different scan vector directions and two different scan vector lengths

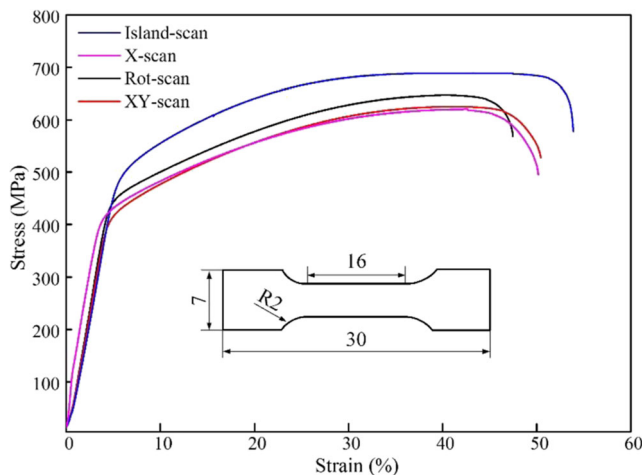


Fig. 6 The stress-strain curves of HASM-manufactured 316L SS specimens at room temperature with different scanning strategies

conducted at room temperature is shown in Fig. 6. The corresponding measured tensile properties, such as ultimate tensile strength (UTS), yield strength (YS), and elongation to failure (ETF), are listed in Table 4. It is clear that all scan strategies presented similar elastic behavior. However, there is a significant difference in the ETF among the X-scan, XY-scan, and Rot-scan samples, with an average engineering elongation of 40.63, 47.63, and 36.69% for the X-scan, XY-scan, and Rot-scan samples, respectively. The increased ductility is attributed to the improvement in the densification (the lack of porosity). Porosity often causes a limited ductility. The XY-scan strategy resulted in the highest UTS and YS values of 649.75 and 429.03 MPa, respectively, while the Rot-scan sample (where the scanning direction alternated 45° with respect to the previous layer) showed the lowest UTS and YS values (620.11 and 386.61, respectively). This can be attributed to the Rot-scan being oriented 45° to the tensile load direction and the weak bulk metallurgical material, which had a heterogeneous particle distribution and decreased densification. The specimens fabricated with the X-scan and Rot-scan patterns demonstrated similar tensile strengths, but the ETFs were quite different. Moreover, the samples with the X-scan and Island-scan patterns had similar ETFs, but the YS and UTS varied greatly across and within the scanning strategy. The residual porosity is an important element that deteriorates the mechanical behavior of HASM-fabricated specimens. Moreover, the anisotropic

Table 4 The mechanical properties of HASM-manufactured 316L SS samples with different scanning strategies

| Scanning strategy | YS | UTS | ETF |
|-------------------|--------|--------|-------|
| X-scan | 399.34 | 625.01 | 40.63 |
| Rot-scan | 386.61 | 620.11 | 36.69 |
| XY-scan | 429.03 | 649.75 | 47.63 |
| Island-scan | 479.18 | 688.37 | 50.25 |

mechanical behavior of the manufactured 316L SS specimens was closely correlated with texture formation. For example, the XY-scan sample had a significantly higher YS, UTS, and ETF and experienced an increased hardening compared with those for the specimens with the X-scan and Rot-scan patterns. This, in turn, was due to the increased uniformity of the particle distribution [29] and improvement in the densification degree. In fact, the XY-scan resulted in a partially disordered direction due to the significant thermal diffusion in the top region. In particular, it is straightforward and effective to adjust the degree of morphological texture by changing the layer thickness (d) and/or hatch spacing (t) because these factors determine the degree of remelting between adjacent layers (a larger d and/or t could decrease their magnitudes and reduce heat accumulation) [4]. The densification level of the Island-scan sample was obviously increased, which further led to an increase in the UTS and YS. Moreover, the ductility increase was attributed to an improvement in the ETF. Generally, the results indicate that the degree of anisotropy in the scan vector direction and scan vector length increase the anisotropy or variation in the mechanical behavior due to a change in the porosity.

To further illuminate the failure mechanisms for the different tensile behaviors among the specimens, the fracture surfaces of the tensile-tested samples fabricated by HASM with different scanning vector directions and lengths were investigated, and the results are shown in Fig. 7. All samples fractured at approximately 45° angles with the load direction. The X-scan, XY-scan, and Rot-scan samples were used to illuminate the different failure mechanisms for the different scanning directions. A low-magnification SEM micrograph of the Rot-scan sample indicated a minimum area reduction compared with that of the other X-scan and XY-scan samples. The XY-scan specimen had an even greater area reduction than that of the X-scan and Rot-scan samples. The area reduction of the X-scan sample was between the two, as shown in Fig. 7a, c. The high-magnification SEM micrographs show the fracture surfaces for a variety of processing parameters, and one can see that the specimens fabricated with HASM and built along different scan directions all exhibited nearly evenly distributed dimples and evidence of tortuous crack growth on the fracture surface, indicating that fairly ductile fracture occurred, as shown in Fig. 8. Pores $\sim 6 \mu\text{m}$ long and second-phase particles were found in the section of the X-scan sample (see Fig. 8a). Compared with the results in Fig. 8a, c, the fracture surface for the Rot-scan sample had localized defects, such as large crater-like voids and noticeable second-phase particles, that could cause local stress concentration, crack propagation, and inhomogeneous heat transfer that could lead to severe degradation in the tensile strength (including the UTS and YS) (see Fig. 8b). The XY-scan sample did not have significant voids and had a homogeneous distribution of dimples on the fracture surface; therefore, the tensile strength was better than that of the other specimens. Given the detrimental influence of pores on the tensile ductility, the absence of porosity (and a high densification

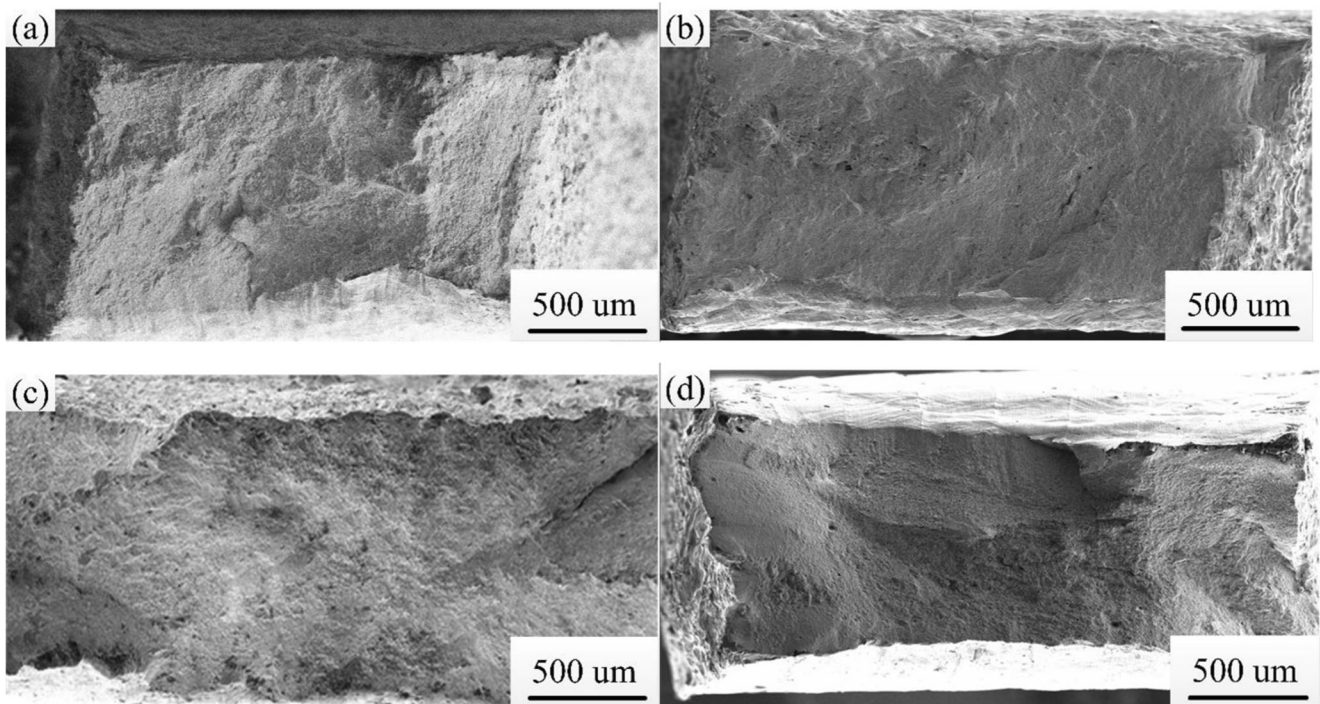


Fig. 7 Low-magnification SEM images exhibiting the fracture surfaces of tensile-tested specimens with different scanning strategies: **a** X-scan; **b** Rot-scan; **c** XY-scan; and **d** Island-scan

level) on the fracture surfaces was indicative of a nearly fully dense material.

To further illuminate the failure mechanisms during the tensile tests of the samples with different scan lengths, the fracture surfaces of the samples fabricated with the XY-scan and $7 \times 7 \text{ mm}^2$ Island-scan patterns were investigated. As shown in Fig. 7d, the $7 \times 7 \text{ mm}^2$ Island-scan had an even greater area reduction than that of the XY-scan (see Fig. 7c). The high-magnification SEM micrograph, which shows the $7 \times 7 \text{ mm}^2$ Island-scan strategy, had an even more uniform fracture surface morphology than that of the XY-scan, as shown in Fig. 8c, d. These trends occurred because the Island-scan had a shorter scan length of $7 \times 7 \text{ mm}^2$ than that of the aforementioned scan strategies. The decreased length of the melt pool could reduce the Rayleigh instabilities and Marangoni forces, which can lead to inappropriate wetting of the melt pool due to the inability of the melt to overcome the surface tension. The flowability and rheological properties of the achieved melt were improved for the island scanning pattern. Therefore, the density of the molten pool was sufficiently high, leading to an increased homogeneity and an efficient mass and heat transfer inside the pool. This can also reduce the porosity induced by the scan strategy that was aligned with the loading axis of the sample.

4 Surface roughness

The use of feasible machining parameters for a given system could dramatically improve the machining quality. The f_z is

one of the most important factors in any type of machining [21]. To research the effect of the f_z on the side surface morphology of the SM process that occurred during the HASM process, the side surfaces of the bulk samples were machined by the CNC milling process that occurred during the HASM process at f_z values of 0.2–0.35 mm. Moreover, the other machining parameters, such as a_p , a_e , and V_s values of 0.5 mm, 0.2 mm, and 120 m/min, respectively, were fixed. The surface roughness is one of the most specified requirements, and the surface roughness was measured by 3D surface profilometry. According to the literature [24–26], 2D surface roughness parameters, such as the profile arithmetic average error Ra, are insufficient to evaluate the surface quality. At present, 3D surface roughness parameters have been developed that are based on the 2D parameters of surface roughness and are widely used in many industrial quality evaluation systems. In this paper, the surface arithmetic mean deviation Sa and the surface maximum height difference Sz were selected to evaluate the milled surface roughness conditions.

As seen in Fig. 9, the surface roughness increased with increasing f_z because as the f_z value increases, the milling thickness, milling force per unit volume, and milling heat per unit time all increase, thereby causing wear of the cutting tools. When the f_z was 0.2 mm, a relatively low surface roughness of Sa = 0.96 μm and Sz = 5.67 μm was achieved for the specimens fabricated with HASM. The reason for this may be that the f_z was too low, the milling thickness was small, and the tool was not worn, so an improved surface roughness was obtained. With an increase in the f_z from 0.2 to 0.3 mm, the

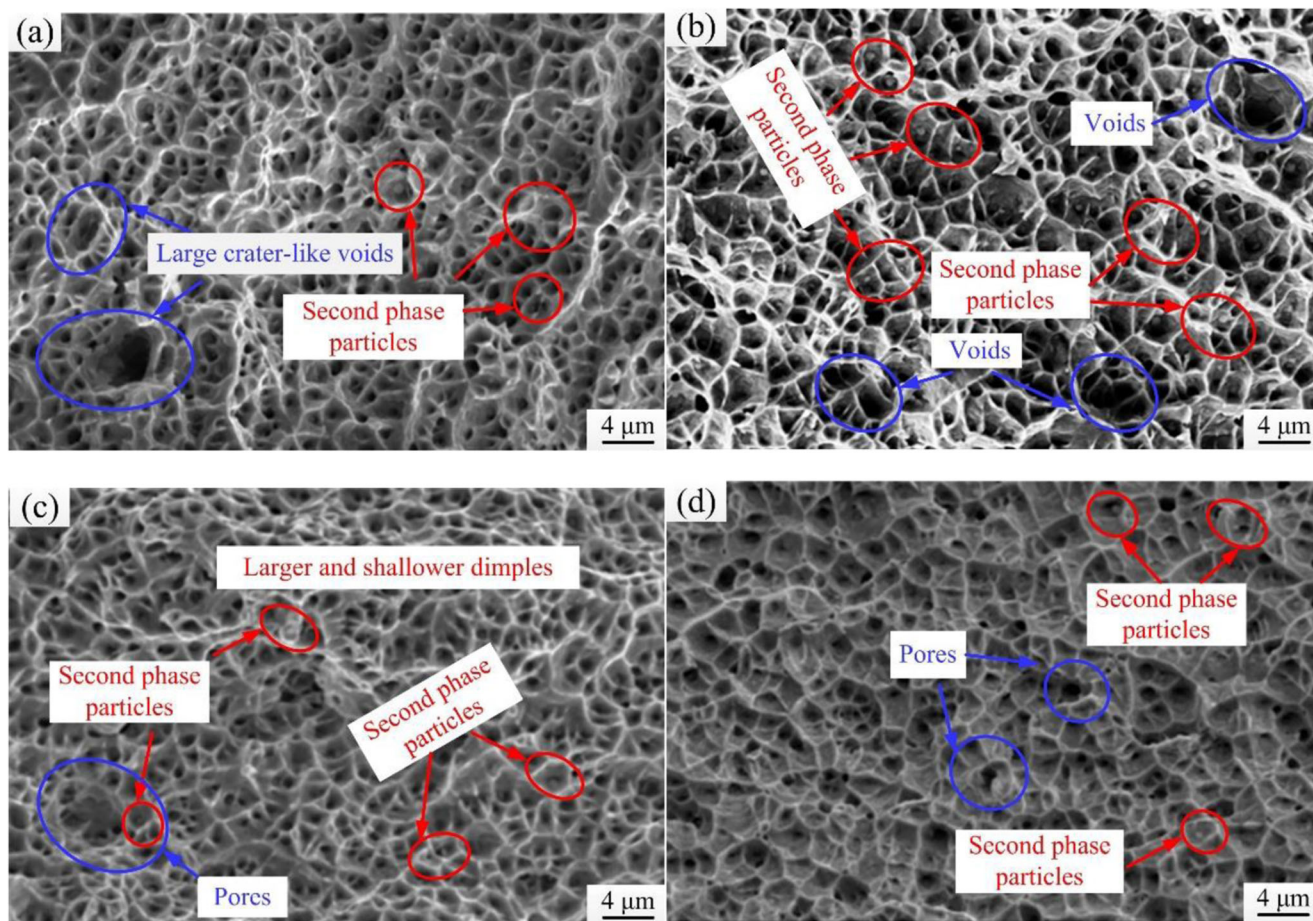


Fig. 8 High-magnification SEM images exhibiting the fracture surfaces of tensile-tested specimens by HASM scanning methods: **a** X-scan; **b** Rot-scan; **c** XY-scan; and **d** Island-scan

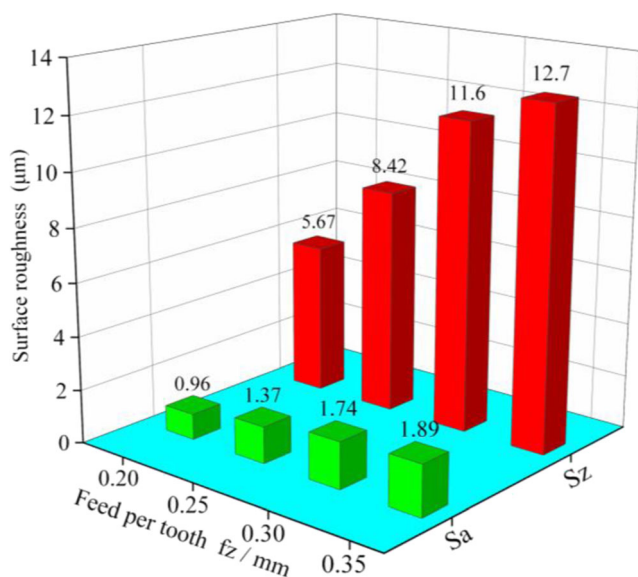


Fig. 9 Surface roughness of subtractive milling process-fabricated 316L SS specimens under incident milling linear speed of 125.6 m/min with various feed per tooth (f_z) change from 0.2 to 0.35 mm

values of S_a and S_z increased from 0.96 to 1.74 μm and 5.67 to 11.6 μm , respectively. This was due to the feed knife trace, cutting load, and layer thickness of the material removal, which all increased with an increase in the f_z value and thereby increasing the vibration and plastic deformation of the material, which in turn deteriorated the surface quality. After increasing the f_z to 0.35 mm, there was almost no change in the surface roughness. The reasons are summarized as follows. On the one hand, the tool wear reached a stable state; on the other hand, the increased f_z made it difficult for the material to adhere to the machined surface. Therefore, the convergence was conducive to reducing the surface roughness. During the HASM process, the CNC milling process can produce a rough or fine process only if the workpiece is fixed on time. The relationship between the f_z and V_s is also linear and negative [18]. A large f_z and small V_s were selected during the rough finishing process to remove the residual oxide layer on the surface. To obtain good surface quality, a low f_z and high V_s should be chosen.

As shown in Fig. 10, the subtractive milled surface topographies on the 316L SS specimens fabricated with HASM

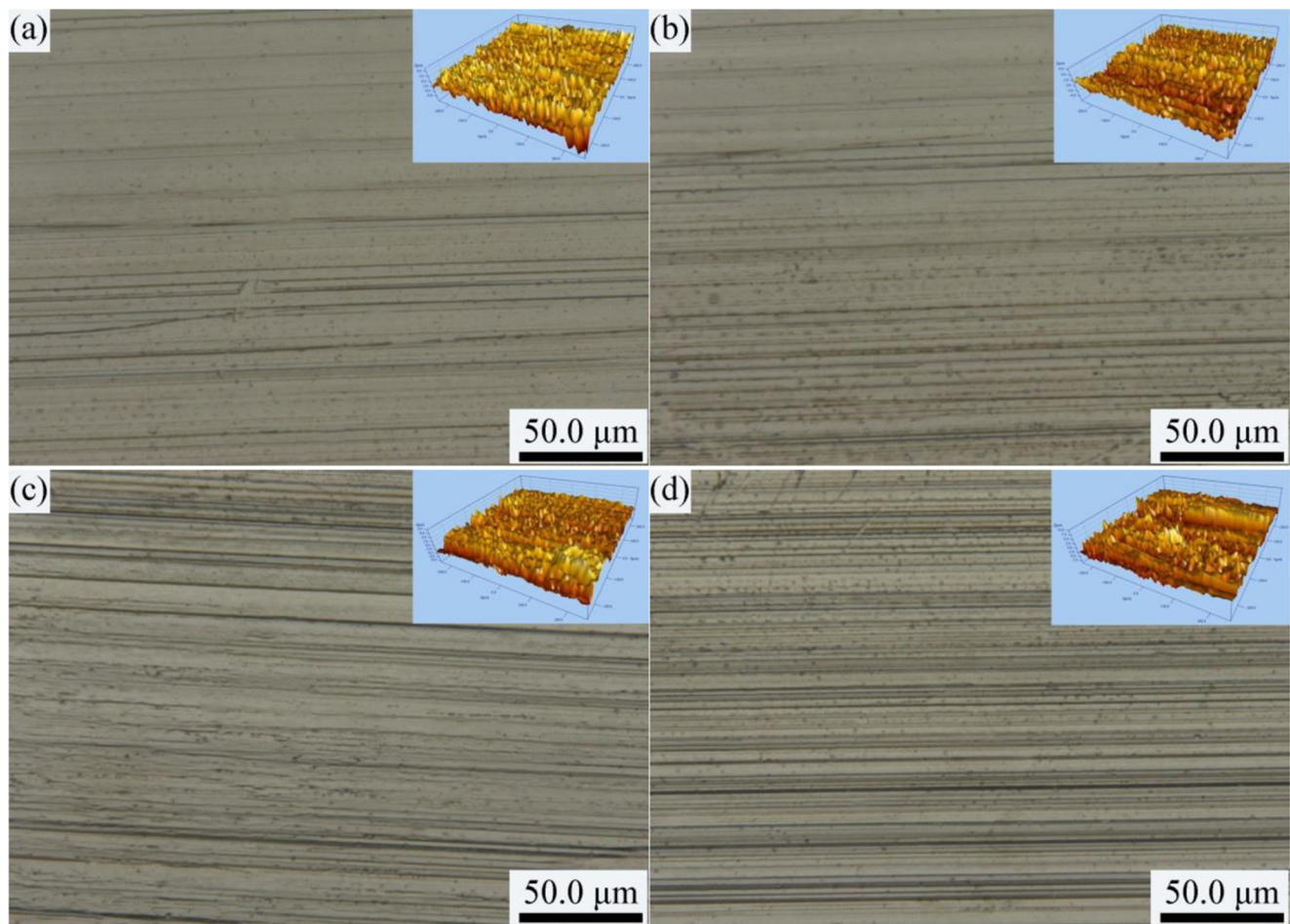


Fig. 10 Surface topographies of subtractive milling process-fabricated 316L SS specimens with various feed per tooth: **a** $f_z = 0.2$ mm, **b** $f_z = 0.25$ mm, **c** $f_z = 0.30$ mm, and **d** $f_z = 0.35$ mm

with various f_z values from 0.2 to 0.35 mm can be understood intuitively. It can be seen that the feed per tooth had an important influence on the milled surface topography. When f_z increased from 0.20 to 0.35 mm, the surface topography of the milled surface gradually deteriorated. The main reason is that as the f_z increased from 0.2 to 0.35 mm, the friction increased the vibration, thereby worsening the surface quality. This means that the best surface quality herein was acquired when the f_z was 0.2 mm. Moreover, large and deep gullies were clearly observed when the f_z was 0.35 mm. Therefore, the trend in the surface topography is consistent with that of the surface roughness.

5 Conclusions

In this paper, the characteristics of 316L SS specimens manufactured by using the HASM method, which combines additive DED manufacturing and a subtractive CNC milling process, were investigated. Four different scan strategies were studied, wherein different scan vector directions (X-scan, Rot-scan, and XY-scan) and vector lengths (Island-scan) were

considered. The effect of the scanning strategies on the densification degree and mechanical behavior was investigated systematically. To improve the surface finish, the influence of the feed per tooth on the surface roughness of the milled 316L SS that was fabricated with HASM was also investigated. The conclusions are as follows.

- (1) Specimens built with the 7×7 mm² Island-scan pattern reached a density of 99.4% and showed a trend of increasing densification compared with that for all three alternating scanning strategies (X-scan, XY-scan, and Rot-scan patterns). This result is attributed to the origin of the pores in the DED process during HASM, such as the inhomogeneous temperature gradient (local heating/cooling of heat source). As a general rule, a body expands when heated and contracts when cooled. Therefore, a decreased scan vector length can reduce the porosity owing to the decreased heat input, moderate thermal gradients, and effective dispersion of heat along multiple directions rather than the accumulation of heat along the building direction. For example, the specimen with the Rot-scan had the highest porosity herein due to

the poor inter-layer bonding that resulted from the short scan vectors on the sides and the long scan vectors in the middle; this condition presented an unstable surface for the scan tracks and residual heat, which increased formation of the pores.

- (2) The hardness value of 251 HV was obtained for specimens manufactured with the $7 \times 7 \text{ mm}^2$ Island-scan, which was higher than that for the other scan strategies. Moreover, the average Vickers hardness on the top surface was lower than that on the side surfaces, and remarkable differences in the Vickers hardness values were achieved for the specimen tops and sides for the specimens fabricated with different scanning strategies. These differences caused the heterogeneous and anisotropic formation of defects associated with the different cooling rates and inhomogeneous heat transfer of different scanning strategies that took place in the DED process during the HASM.
- (3) The XY-scan specimen exhibited improved tensile properties, including a higher UTS, YS, and ductility than that of the 316L SS samples fabricated with the X-scan and Rot-scan patterns, because of the reduced heterogeneous heat accumulation, improved particle distribution uniformity, and improved densification.
- (4) To improve the surface quality during the milling machining that occurs during the HASM process, a small f_z should be selected. The surface roughness decreased with increasing f_z . This is due to the feed knife trace, cutting load, and layer thickness of material removal, which all increased as the f_z increased, thereby increasing vibration and material plastic deformation, which in turn deteriorated the surface quality.

Funding information The author wishes to thank the National Natural Science Foundation of China (No. 51775100) and the Fundamental Research Funds for the Central Universities of China (No. N180306001 and N170313025) for financial assistance.

References

1. Gray GT, Livescu V, Rigg PA, Trujillo CP, Cady CM, Chen SR, Carpenter JS, Lienert TJ, Fensin SJ (2017) Structure/property (constitutive and spallation response) of additively manufactured 316L stainless steel. *Acta Mater* 138:140–149
2. Harrison NJ, Todd I, Mumtaz K (2015) Reduction of micro-cracking in nickel superalloys processed by selective laser melting: a fundamental alloy design approach. *Acta Mater* 94:59–68
3. Gu DD, Meiners W, Wissenbach K, Poprawe R (2012) Laser additive manufacturing of metallic components: materials, processes and mechanisms. *Int Mater Rev* 57(3):133–164
4. Contaldi V, Del Re F, Palumbo B, Squillace A, Corrado P, Di Petta P (2019) Mechanical characterisation of stainless steel parts produced by direct metal laser sintering with virgin and reused powder. *Int J Adv Manuf Technol* 105(7–8):3337–3351
5. Akbari M, Kovacevic R (2019) Closed loop control of melt pool width in robotized laser powder-directed energy deposition process. *Int J Adv Manuf Technol* 104(5–8):2887–2898
6. Jhang SS, Lo YL, Le TN (2019) Systematic modeling approach for analyzing the powder flow and powder energy absorptivity in direct energy deposition system. *Int J Adv Manuf Technol*. <https://doi.org/10.1007/s00170-019-04441-3>
7. Wang ZQ, Palmer TA, Beese AM (2016) Effect of processing parameters on microstructure and tensile properties of austenitic stainless steel 304L made by directed energy deposition additive manufacturing. *Acta Mater* 110:226–235
8. AlMangour B, Yang JM (2017) Understanding the deformation behavior of 17–4 precipitate hardenable stainless steel produced by direct metal laser sintering using micropillar compression and TEM. *Int J Adv Manuf Technol* 90(1–4):119–126
9. Ning JQ, Sievers DE, Garmestani H, Liang SY (2019) Analytical modeling of transient temperature in powder feed metal additive manufacturing during heating and cooling stages. *Applied Physics A* 125:496
10. Ning JQ, Liang SY (2018) Model-driven determination of Johnson-Cook material constants using temperature and force measurements. *Int J Adv Manuf Technol* 97(1–4):1053–1060
11. Zhou YG, Ma LJ, Gong YD, Zhang L, Yin GQ, Sun Y (2019) Study on the mechanism of chip forming and the microhardness of micro-grinding nickel-based single-crystal superalloy. *Int J Adv Manuf Technol* 103(1–4):281–295
12. Pace ML, Guarnaccio A, Dolce P, Mollica D, Parisi GP, Lettino A, Medici L, Summa V, Ciancio R, Santagata A (2017) 3D additive manufactured 316L components microstructural features and changes induced by working life cycles. *Appl Surf Sci* 418:437–445
13. Yadollahi A, Shamsaei N, Thompson SM, Seely DW (2015) Effects of process time interval and heat treatment on the mechanical and microstructural properties of direct laser deposited 316L stainless steel. *Mat Sci Eng A* 644:171–183
14. Yang YY, Gong YD, Qu SS, Rong YL, Sun Y, Cai M (2018) Densification, surface morphology, microstructure and mechanical properties of 316L fabricated by hybrid manufacturing. *Int J Adv Manuf Technol* 97(5–8):2687–2696
15. Le VT, Paris H, Mandil G (2017) Environmental impact assessment of an innovative strategy based on an additive and subtractive manufacturing combination. *J Clean Prod* 164:508–523
16. Ye ZP, Zhang ZJ, Jin X, Xiao MZ, Su JZ (2017) Study of hybrid additive manufacturing based on pulse laser wire depositing and milling. *Int J Adv Manuf Technol* 88(5–8):2237–2248
17. Zhao YH, Sun J, Li JF, Wang PF, Zheng ZC, Chen JW, Yan YQ (2018) The stress coupling mechanism of laser additive and milling subtractive for FeCr alloy made by additive-subtractive composite manufacturing. *J Alloy Compd* 769:898–905
18. Wei P, Wei ZY, Chen Z, Du J, He YY, Li JF, Zhou YT (2017) The AlSi10Mg samples produced by selective laser melting: single track, densification, microstructure and mechanical behavior. *Appl Surf Sci* 408:38–50
19. Qiu CL, Adkins NJE, Attallah MM (2016) Selective laser melting of Invar 36: microstructure and properties. *Acta Mater* 103:382–395
20. AlMangour B, Grzesiak D, Yang JM (2017) Scanning strategies for texture and anisotropy tailoring during selective laser melting of TiC/316L stainless steel nanocomposites. *J Alloy Compd* 728:424–435
21. Xiong XH, Zhang HO, Wang GL (2009) Metal direct prototyping by using hybrid plasma deposition and milling. *J Mater Process Tech* 209(1):124–130
22. Zhu HH, Fuh JYH, Lu L (2007) The influence of powder apparent density on the density in direct laser-sintered metallic parts. *Int J Mach Tool Manu* 47(2):294–298

23. Xiong W, Hao L, Li Y, Tang DN, Cui Q, Feng ZY, Yan CZ (2019) Effect of selective laser melting parameters on morphology, microstructure, densification and mechanical properties of supersaturated silver alloy. *Mater Design* 170:10769711
24. Qu SS, Gong YD, Yang YY, Sun Y, Wen XL, Qi Y (2020) Investigating Minimum Quantity Lubrication in Unidirectional Cf/SiC composite grinding. *Ceram Int* 46:3582–3591
25. Qu SS, Gong YD, Yang YY et al (2019) Grinding characteristics and removal mechanisms of unidirectional carbon fibre reinforced silicon carbide ceramic matrix composites. *Ceram Int* 45:3059–3071
26. Gong YD, Qu SS, Yang YY, Liang CY, Li PF, She YB (2019) Some observations in grinding SiC and silicon carbide ceramic matrix composite material. *Int J Adv Manuf Technol*
27. Woo W, Kim DK, Kingston EJ, Luzin V, Salvemini F, Hill MR (2019) Effect of interlayers and scanning strategies on through-thickness residual stress distributions in additive manufactured ferritic-austenitic steel structure. *Mat Sci Eng A* 744:618–629
28. Nadammal N, Cabeza S, Mishurova T, Thiede T, Kromm A, Seyfert C, Farahbod L, Haberland C, Schneider JA, Portella PD (2017) Effect of hatch length on the development of microstructure, texture and residual stresses in selective laser melted superalloy Inconel 718. *Mater Design* 134:139–150
29. Sun SH, Hagihara K, Nakano T (2018) Effect of scanning strategy on texture formation in Ni-25 at.%Mo alloys fabricated by selective laser melting. *Mater Design* 140:307–316

Publisher's note Springer Nature remains neutral with regard to jurisdictional claims in published maps and institutional affiliations.